

Article

Predicting Liquid Water Condensation in PEM Fuel Cells by Coupling CFD with 1D Models

Maximilian Schmitz *, Fynn Matthiesen, Steffen Dirkes and Stefan Pischinger

Chair of Thermodynamics of Mobile Energy Conversion Systems (TME), RWTH Aachen University,
Forckenbeckstraße 4, 52074 Aachen, Germany

* Correspondence: schmitz_max@tme.rwth-aachen.de

Abstract: Proton exchange membrane fuel cells are a promising technology for future transportation applications. However, start-up procedures that are not optimized for low temperatures can lead to the early failure of the cells. Detailed CFD models can support the optimization of cold start procedures, but they often cannot be solved in a stable way due to their complexity. One-dimensional (1D) models can be calculated quickly but are simplified so that the behavior of the cells can no longer be determined accurately. In this contribution, a coupling between a 2D CFD model of the gas channels and a 1D model of the Membrane Electrode Assembly (MEA) is realized. This method allows not only to determine the location and amount of the condensed water but also to calculate the exact concentration of the reactant gases along the channels. The investigations show that the concentrations of the gases and the relative humidities in the gas channels are strongly influenced by the current density. It has been found that it is not possible to avoid the formation of liquid water at low operating temperatures by controlling the current density.

Keywords: proton exchange membrane fuel cell; cold start; water condensation; model coupling; computational fluid dynamics; low temperature operation; membrane electrode assembly; relative humidity; current density control



Citation: Schmitz, M.; Matthiesen, F.; Dirkes, S.; Pischinger, S. Predicting Liquid Water Condensation in PEM Fuel Cells by Coupling CFD with 1D Models. *Energies* **2024**, *17*, 1259. <https://doi.org/10.3390/en17051259>

Academic Editor: Antonino S. Aricò

Received: 9 February 2024

Revised: 23 February 2024

Accepted: 26 February 2024

Published: 6 March 2024



Copyright: © 2024 by the authors. Licensee MDPI, Basel, Switzerland. This article is an open access article distributed under the terms and conditions of the Creative Commons Attribution (CC BY) license (<https://creativecommons.org/licenses/by/4.0/>).

1. Introduction

One of the biggest advantages of PEM fuel cells is that they only produce pure water as exhaust gas during operation. This makes them a promising future alternative to conventional combustion engines in transportation applications. However, depending on the local temperature and pressure, the water can condense. During cold starts, at temperatures above the freezing point of water, large amounts of liquid water can cause local flooding. Flooding hinders gas transport, which leads to starvation and thus reduces the performance, efficiency, and lifetime of the fuel cell. At temperatures below the freezing point, liquid water droplets freeze to ice. During such a freeze start, ice formation also blocks gas transport and leads to lower current density production [1]. At the same time, ice formation leads to local mechanical stress peaks in the cell layers, which can damage the cells by deteriorating their structural properties or even destroying them [2]. In order to heat the cells as quickly as possible at low temperatures, high current densities are set during the starting process. The high current densities also generate a large amount of heat, which causes the cells to heat up more quickly. The disadvantage is that a lot of water is produced at the same time, which causes the effects described. This correlation makes it clear that water management is critical during a cold start [3].

For the widespread establishment of fuel cell vehicles, the cold start issues must be solved or significantly improved. For this purpose, the development of simulation models is required to better understand and predict the phase change processes. Numerical flow simulations can help to predict, at the earliest possible stage of development, the location and amount of condensate in the gas channels. Detailed multi-dimensional flow

calculations are computationally expensive and cannot always be solved in a stable way. For this purpose, simplifications are necessary in order to achieve sufficiently accurate results at a reasonable cost. CFD simulations of an entire cell are therefore not always appropriate.

In this study, a new method is presented that allows for the determination of the concentrations of the reactants and the condensation of liquid water in the gas channels of a PEM fuel cell under cold start conditions. In order to avoid a detailed multi-physics CFD model, a coupling between a one-dimensional model of the MEA, which, among other things, calculates the electrochemistry, and a CFD model of the gas channels is realized. This results in a model that is simple and stable to solve but nevertheless exhibits high accuracy. Since the simulation software used does not have a suitable interface for the coupling, an algorithm is developed that enables the coupling via the periodic exchange of .csv files. In each iteration step, information is exchanged between both softwares in this way.

2. Literature Research

Even before Springer et al. and Zawodzinski et al. conducted measurements of membrane water uptake, protonic conductivity, and electroosmotic drag in PEM fuel cells, which are important for modeling, researchers were engaged in modeling the performance and water management of PEM fuel cells [4,5]. The first mathematical models that investigated important water management only used spatial resolution for the direction through the membrane and the gas diffusion layers and therefore assumed well-mixed gas channels [6,7]. Firstly, Fuller and Newman [8] use the idea of a two-dimensional investigation by integrating the determined water profile downstream of the co-flow arrangement. Despite the fact that the resolution cannot compete with commercial numerical solvers nowadays, these publications give insights into the performance of the membrane under different current density loads [8].

Nguyen and White extend a previously presented two-dimensional model that accounts for channel flow and membrane transport [9]. Although the spatial resolution along the gas channels is good, the grid size across the membrane remains unclear. The publication aims to predict the water management by different humidification systems and the partial pressure profiles along the channel for different cases [9]. The modeled fuel cell changes temperature along the channel and is therefore not isothermal, adding complexity to the model [9]. Despite the greater complexity of the model, the real behavior is better represented by the non-uniform temperature distribution. Since a degradation in performance can be observed due to the non-uniform distribution, a non-isothermal assumption is an important boundary condition for an accurate model [10]. Nguyen and White find that the hydrogen partial pressure increases along the anode channel, despite the consumption of hydrogen by the cell reaction [9].

Possibly the first fully two-dimensional model with a high resolution of the gas channels and the gas diffusion layers is presented by Gurau et al. [11]. Assumptions on fluid flow, such as negligible pressure losses along the channel and laminar flow, are considered for the first time. The diffusion coefficients are based on the Stefan-Maxwell equations, and the Navier-Stokes equations are solved numerically. Since they model the fluid flow in more detail than previous authors, Gurau et al. are able to study important fuel cell performance parameters such as cell temperature, flow velocities, and GDL porosities. The concentrations of water vapor and oxygen are shown for various predefined current densities in the GDL and gas channels [11].

A fully three-dimensional fuel cell model is presented by Dutta et al. [12]. The authors extend the Navier-Stokes equations in the commercial software ANSYS Fluent with source terms to implement electrochemistry and membrane sorption. Since the experimentally studied fuel cell of Dutta et al. shows high thermal inertia, they compare their results to the measurements of Fuller and Newman [8]. The authors use their model to study the current density distribution on the electrochemically active membrane surface. To do so, they use isothermal, steady-state, and single-phase assumptions to facilitate the solution. For the

studies, the gas channels are flowed through in parallel since opposite flow directions in the anode and cathode significantly increase numerical effort [13].

Natarajan and Nguyen present a quasi-three-dimensional fuel cell model based on their earlier work to predict the transport of liquid water and the reaction gases on the cathode side of a fuel cell [14,15].

In recent years, several lumped or spatially resolved fuel cell models have been developed in MATLAB/Simulink, which have the great advantage of providing accurate insights into the local distributions with low computational effort [16–18].

Chen and Peng use a 15-segment approach within the fuel cell to track water formation and current density distribution for different flow fields. Simulation results are compared to measured segmented current density distributions [17,19].

In contrast, Gray et al. develop a one-dimensional fuel cell model in Simulink and compare their simulated voltage curves with experimental data from other studies. Remarkably, their model is able to predict these polarization curves very well despite the lack of complex spatial resolution [16].

A different approach to modeling different cell regions is taken by Schumacher et al. The gas channels are simulated individually, and the conditions at the surfaces of the GDLs are transmitted to a second model that calculates diffusion and electrochemistry [20].

Pant et al. publish another pseudo-3D (1D + 2D) model with one-dimensional resolution of the gas channels and two-dimensional resolution of the MEA processes. Also, in this case, two models are used that exchange data with each other. The one-dimensional and two-dimensional models are each created in different software. As both software programs have an interface to each other, the coupling between the two models is simplified [21].

3. Theoretical Formulation

For the purposes of this study, a two-dimensional model of the gas channels is coupled to a one-dimensional model of the MEA. Both models are solved in a co-simulation.

A single gas channel of the anode and a single channel of the cathode are modeled. The gas channels are implemented in the commercial CFD tool, Siemens Star-CCM+ 13.06. The 1D model of the MEA is created in the commercial tool MATLAB/Simulink R2018b.

For the coupling, the surfaces of the gas diffusion layers (GDLs) represent the interfaces between both models. The coupling is schematically shown in Figure 1. The model of the MEA receives the partial pressures of all gas components on the surfaces of the GDLs inside the gas channels from the CFD model and thus calculates the electrochemistry and mass flows of the components, which are exchanged between both models during the operation of the cell. With the help of the determined mass flows, the CFD model determines the distribution of the gas components along the gas channels. In the simulations, it is assumed that all components involved in the reaction are only present in the gaseous state. Water vapor can condense out when the saturation vapor pressure is exceeded, but liquid water is not modeled as a separate phase in the simulations. The location and quantity of condensation are determined purely by the thermodynamic conditions of the gas phase, i.e., relative humidity, pressure, and temperature. For this reason, the very complex and unstable implementation of additional equations describing the transport of liquid water can be avoided. The models consider hydrogen, oxygen, nitrogen, and water vapor. In the following sections, a detailed description of the models is given. The variable names are given in the Nomenclature section at the end of this paper, and the parameter values used can be found in Table A1.

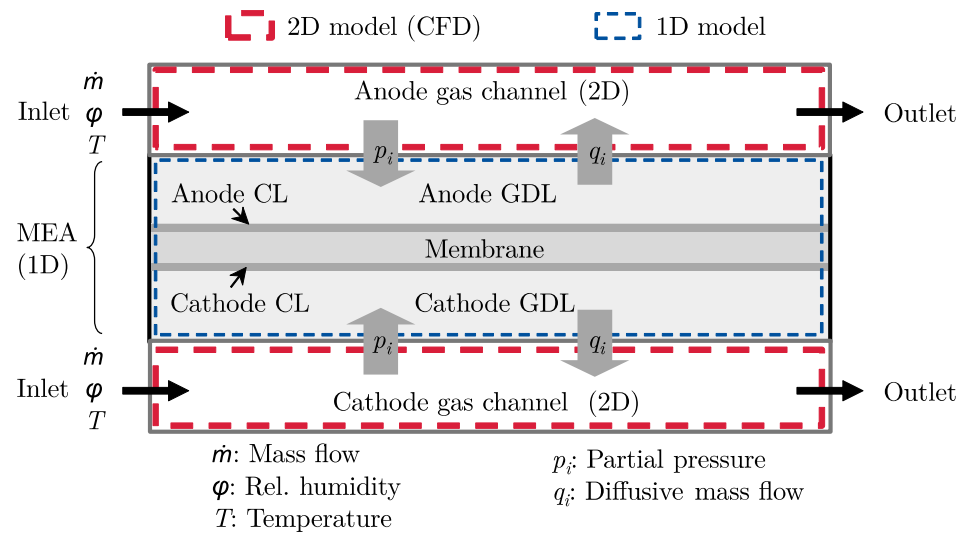


Figure 1. Coupling between the 2D CFD model of the gas channels and the 1D model of the MEA. The partial pressures of the gas components in the channels and the mass fluxes diffusing through the surface of the GDLs are exchanged between the two models (for reasons of simplicity, the MPLs are not shown in this figure).

3.1. One-Dimensional Model of MEA

In order to simulate the production of electrical energy and water, as well as the consumption of hydrogen and oxygen, a one-dimensional model of the MEA is created. The model calculates the cell voltage and the exchanged mass flows through the surfaces of the GDLs from the demanded cell current density and the partial pressures of the gas components in the channels of the anode and cathode.

The model is built galvanostatically, i.e., a current density is given, and from this, the cell voltage is determined.

The cell voltage and the maximum cell current density depend strongly on the concentrations of the species involved in the reaction in the catalytic layers (CLs). The cell voltage is composed of the Nernst voltage minus several voltage losses and is calculated as follows [22,23]:

$$U_{Cell} = U_{Nernst} - \Delta U_{mix} - \Delta U_{act} - \Delta U_{\Omega} \quad (1)$$

The diffusion losses result indirectly from this representation because the Nernst voltage and the activation losses depend on the respective concentrations in the catalyst layers. Since the decrease in concentrations due to diffusive gas transport is calculated in detail, this influence is also included. The Nernst voltage results from [24]:

$$U_{Nernst} = U^0 + \frac{\Delta S_R^0}{2nF} \cdot (T - T_{ref}) + \frac{RT}{2nF} \cdot \ln \left(\frac{\left(\frac{p_{H_2}}{p^0} \right)^2 \cdot \frac{p_{O_2}}{p^0}}{\left(\frac{p_{H_2O}}{p^0} \right)^2} \right) \quad (2)$$

The mixed voltage losses ΔU_{mix} are caused by hydrogen transfer from the anode to the cathode. This value is estimated during the calibration of the model with measurements.

The activation overvoltage at the cathode is much higher than at the anode, and due to simplification, the anodic overvoltage is neglected to be able to transform the Butler-Volmer equation to the cathode overvoltage [22]:

$$\Delta U_{act} = \frac{RT}{2\alpha nF} \cdot \operatorname{arcsinh} \left[\left(\frac{p_{H_2O}}{p^0} \right)^2 \cdot \frac{p^0}{p_{O_2}} \cdot \frac{i''}{2 \cdot i''_{0,ORR}} \cdot \exp \left(\frac{\Delta E_{act,ORR}}{R_m} \cdot \left(\frac{1}{T} - \frac{1}{T_{ref}} \right) \right) \right] \quad (3)$$

Here $i''_{0,ORR}$ stands for the cathodic exchange current density, and the activation energy $\Delta E_{act,ORR}$ determines the influence of different cell temperatures on the exchange current density. The exchange current density is strongly dependent on temperature; it increases with increasing temperature, following the Arrhenius law. p_{H_2O} and p_{O_2} are the partial pressures of hydrogen and oxygen in the anodic and cathodic catalytic layer, respectively. p^0 is the reference partial pressure.

The ohmic voltage losses are composed of the losses due to electrical resistances in the cell layers and the bipolar plates and of the losses due to the protonic resistance of the membrane [25]:

$$U_{\Omega} = (R_{elec,GDL,BPP} + R_{prot,mem}(\lambda_{mem}, T)) \cdot i_{cell} \quad (4)$$

Here $R_{elec,GDL,BPP}$ stands for the sum of all electrical resistances in the cell materials and due to contact resistances between the cell layers and the bipolar plates. The protonic resistance of the membrane $R_{prot,mem}(\lambda_{mem}, T)$ is determined as follows [4,26]:

$$R_{prot,mem}(\lambda_{mem}, T) = \frac{d_{mem}}{(0.5139 \cdot \lambda_{mem} - 0.326) \cdot \exp\left(1268 \text{ K} \cdot \left(\frac{1}{303 \text{ K}} - \frac{1}{T}\right)\right)} \quad (5)$$

d_{mem} is the thickness and λ_{mem} the average water content of the membrane.

To solve Equations (2) and (3), the partial pressures of the gas components in the CLs are required. These are determined by mass balances around the CLs for each component:

$$p_{CL,i} = \int \frac{RT}{M_i \cdot V_{CL}} \cdot (\dot{m}''_{prod,i} + \dot{m}''_{cons,i} + \dot{m}''_{mem,i} + \dot{m}''_{GC2CL,i}) dt \quad (6)$$

V_{CL} is the porous gas volume of the respective CL, M_i is the molar mass of the balanced substance, and $\dot{m}''_{GC2CL,i}$ is the area-related mass flow rate, which flows into or out of the CL from the gas channel. For the gas components hydrogen H_2 , oxygen O_2 and water H_2O , further mass flows due to consumption and production must be considered. Further source terms stand for diffusion and transport through the membrane in the case of H_2 and nitrogen N_2 . Production and consumption are derived from Faraday's law as a function of the current density i'' [27]:

$$\dot{m}''_{cons,H_2} = -\frac{M_{H_2} \cdot i''}{2F} \quad (7)$$

$$\dot{m}''_{cons,O_2} = -\frac{M_{O_2} \cdot i''}{4F} \quad (8)$$

$$\dot{m}''_{prod,H_2O} = \frac{M_{H_2O} \cdot i''}{2F} \quad (9)$$

Due to the concentration gradient of the gases between the CL and the gas channel, a diffusive mass transfer occurs. This is determined in a simplified way with Fick's law and constant diffusion coefficients [22]:

$$\dot{m}''_{GC2CL,i} = \frac{1}{d_{eff}} \cdot \frac{M_i}{RT} \cdot D_{MEA,i} \cdot \frac{\varepsilon}{\tau} \cdot (p_{GC,i} - p_{CL,i}) \quad (10)$$

$p_{GC,i}$ and $p_{CL,i}$ denote the partial pressures of the gas component i in the gas channel and in the catalytic layer, respectively. d_{eff} is the average diffusion path from the channel into the CL. The diffusion path is larger for the supply of the CLs under the ribs of the bipolar plate. This equation is corrected by the porosity ε and the tortuosity τ of the porous cell layers.

Water transport through the membrane results from a superposition of water diffusion and the transport by electro-osmotic drag [27]:

$$\dot{m}_{H_2O,i}'' = \frac{2.5 \cdot \lambda}{22} \cdot \frac{i_{cell} \cdot M_{H_2O}}{F} + \rho_{mem} \cdot \frac{M_{H_2O}}{M_{mem} d_{mem}} \cdot D_\lambda \cdot 10^{-4} \cdot \exp\left(1268 \cdot \left(\frac{1}{303 K} - \frac{1}{T}\right)\right) \cdot (\lambda_{mem,A} - \lambda_{mem,C}) \quad (11)$$

D_λ represents the diffusion coefficient of solved water in the membrane and is derived from [27]. O_2 and H_2 diffusion through the membrane can be neglected in this model [7].

The membrane water content is generally defined as the number of water molecules bound per sulfonic acid end group of the membrane material. The membrane water content is determined by the following empirical equation from the relative humidity RH of the surrounding gas [4,28]:

$$\lambda_{mem}(RH) = 0.043 + 17.81 \cdot RH - 39.85 \cdot RH^2 + 36 \cdot RH^3$$

Due to the ribs of the bipolar plates, which cover large parts of the surfaces of the gas diffusion layers, the diffusion of the gases from the channels to the CL (and vice versa) is hindered. This leads to a poor supply of the areas under the ribs, which results in a lower current density. This effect is considered in the model by dividing the MEA model internally into two areas—the area under the gas channel and the area under the rib. The only difference between both areas is a significantly longer diffusion path d_{eff} to the CLs under the rib.

3.2. Two-Dimensional Model of Gas Channels

To improve stability and reduce computational effort, the gas channels on the anode and cathode sides are simplified to be two-dimensional. This assumption is valid because the main flow direction of the gases in the channels is along the length of the channels, and the main diffusion direction of the gas components is perpendicular to that direction and the surfaces of the gas diffusion layers. Thus, the transport of the species takes place only in both directions, and transport in the cross direction can be neglected. The flow directions in the channels are assumed to be parallel.

The model is implemented isothermally so that only the continuity equation and the conservation of momentum equations have to be solved [29]:

Continuity equation:

$$\nabla \cdot (\varepsilon \cdot \rho_{gas} \cdot \vec{v}_{gas}) = \varepsilon \cdot \dot{S}_m \quad (12)$$

Conservation of momentum equations [29]:

$$\nabla \cdot (\varepsilon \cdot \rho_{gas} \cdot \vec{v}_{gas} \cdot \vec{v}_{gas}) = -\varepsilon \cdot \nabla p + \nabla \cdot (\varepsilon \cdot \bar{\tau}) \quad (13)$$

with:

$$\bar{\tau} = \mu \cdot \left[\left(\nabla \vec{v}_{gas} + \nabla \vec{v}_{gas}^T \right) - \frac{2}{3} \cdot \nabla \cdot \vec{v}_{gas} \cdot I \right] \quad (14)$$

The convective flow is additionally overlapped by the diffusion of the gas species [29]:

$$\nabla \cdot (\varepsilon \cdot \rho_{gas} \cdot \vec{v}_{gas} \cdot Y_i) = -\nabla \cdot (\varepsilon \cdot \rho_{gas} \cdot D_{m,i} \cdot \nabla Y_i) + \varepsilon \cdot \dot{S}_i \quad (15)$$

Y_i is the mass fraction of component i , \vec{v}_{gas} is the flow velocity, ρ_{gas} is the density of the fluid, and \dot{S}_i is the source and sink terms of species i . J_i stands for the diffusive mass flow, which is determined with the Maxwell-Stefan equations. The Maxwell-Stefan equations

determine the diffusion in multicomponent mixtures and are calculated in isothermal mixtures by [29]:

$$\nabla X_i = \frac{M_w}{\rho} \cdot \sum_{j=1, j \neq i}^n \frac{X_i J_j}{M_j D_{i,j}} - \frac{X_j J_i}{M_i D_{i,j}} \quad (16)$$

Here, X_i stands for the mole fractions, M_w for the mean molar mass, M_i or M_j for the molar masses of the substances i or j , and $D_{i,j}$ are the binary diffusion coefficients. The binary diffusion coefficients are determined by the Kinetic Theory of gases [29].

The mass fraction of the fourth component is given by the closing condition:

$$1 = \sum Y_i \quad (17)$$

Due to the low Reynolds numbers in the channels, a laminar flow is assumed for both channels, and the behavior of the gases is approximated by the Ideal Gas Law. Both channels have a length of 650 mm and a height of 1 mm.

Although liquid water is not modeled, as soon as the partial pressure of the water vapor exceeds the saturation vapor pressure, it is assumed that water condenses out. The condensation is implemented as a volume-related mass flow sink, which reduces the existing mass of water vapor. As long as the partial pressure of the water vapor is lower than the saturation vapor pressure, this mass flow is zero. However, if the partial pressure rises above the saturation vapor pressure, the mass flow of the condensing water is determined by the following relationship [30]:

$$\dot{m}''_{cond} = C \cdot (p_{H_2O} - p_{sat}) \quad (18)$$

The constant C can be poorly determined physically since condensation depends on many factors, such as temperature, porosity, hydrophobicity of the diffusion layers, and the presence of suitable condensation nuclei. In accordance with the phase change law from [31], the constant is estimated to be $C = 6 \cdot 10^{-3} \text{ kg} \cdot \text{s}^{-1} \cdot \text{m}^{-3}$. This value is large enough so that the relative humidity does not exceed 105% and small enough so that stable solving of the model is ensured.

3.3. Coupling between MEA and Channel Model

The coupling and the data exchange between the MEA model and the channel model are illustrated in Figure 2. To link the one-dimensional MEA model with the two-dimensional model of the gas channels, the gas channels must first be divided into virtual sections along the channels. Since the concentrations of the gases vary over the channel length and these concentrations significantly influence the cell voltage, the MEA model must be solved once for each segment per iteration step of the CFD model. For each segment, an average value is formed from the continuous course of the gas concentrations in the CFD model, which is given to the MEA model.

A division into 10 segments is used for the investigations in this study. Simulations for comparison with 20 segments have shown that there is no significant difference between 10 and 20 segments.

Due to the flow distributor and the collector within the bipolar plates, the gas channels are modeled 15 mm longer at the beginning and end than they actually are. At these extensions, there is no exchange with the model of the MEA since these areas are not activated. The inlet sections ensure that the flow profile is fully formed as soon as the exchange with the model of the MEA begins. This ensures higher numerical stability for the simulations.

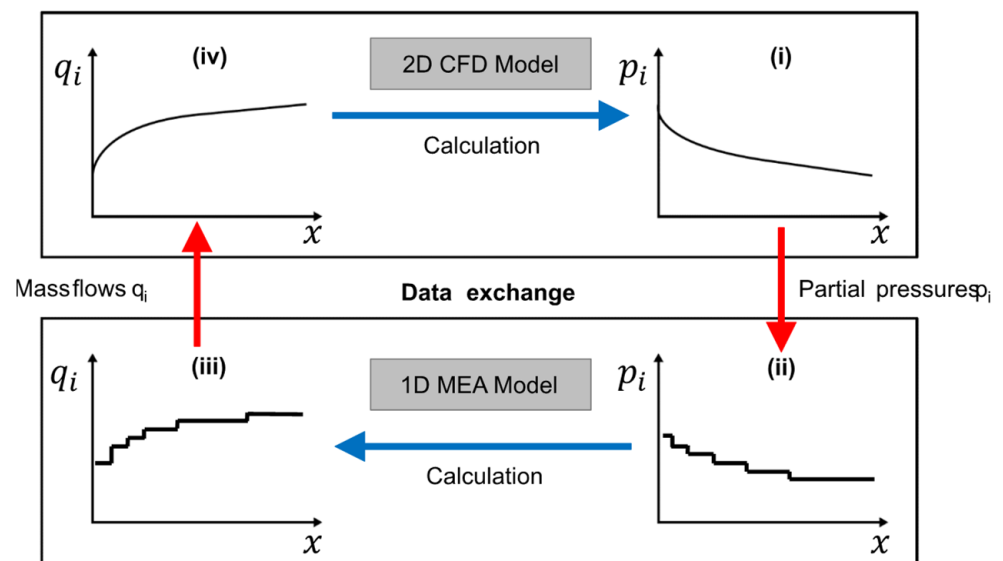


Figure 2. Schematic representation of the coupling between the one-dimensional model of the MEA and the two-dimensional CFD model of the gas channels. The MEA model is applied to discrete segments along the gas channels. For the data exchange, average values are formed over these segments.

In the first step of the coupling algorithm, the continuous curves of the partial pressures along the channel are transformed as described into a step-shaped average profile ((i) to (ii)). Since the MEA model is simulated for each segment, a step-shaped curve of the exchanged mass flow rates is solved ((ii) to (iii)). With the help of linear interpolation, the curves of the mass flow rates are then smoothed and specified as a boundary condition for the CFD model ((iii) to (iv)). Based on this, the CFD model determines the continuous profiles of the partial pressures ((iv) to (i)). This procedure is repeated until the solution has converged and the values change by less than 0.05% per iteration. In order to increase the stability of the process and speed up convergence, the described coupling algorithm is performed not in each iteration of the CFD model but every 20 iterations. Due to the type of coupling, both models are not calculated in parallel but alternately.

Since there is no suitable interface between MATLAB and Star-CCM+, the coupling of both models must be realized with the help of custom control scripts. The Simulink model of the MEA is controlled by a MATLAB script. The control of the CFD model requires a Java script. The data exchange between the two models is achieved by a .csv file, which is overwritten after each computation of one model and is then imported into the other model. The .csv data type is suitable for this purpose because it can be imported and exported for both MATLAB and Star-CCM+. The control scripts are implemented in such a way that one model waits until the other model has completed its calculation step. Then the files are exchanged, and the next calculation begins. This cycle is repeated until a stationary converged solution of the H_2 and O_2 distributions are reached. A schematic diagram of this coupling algorithm is shown in Figure 3.

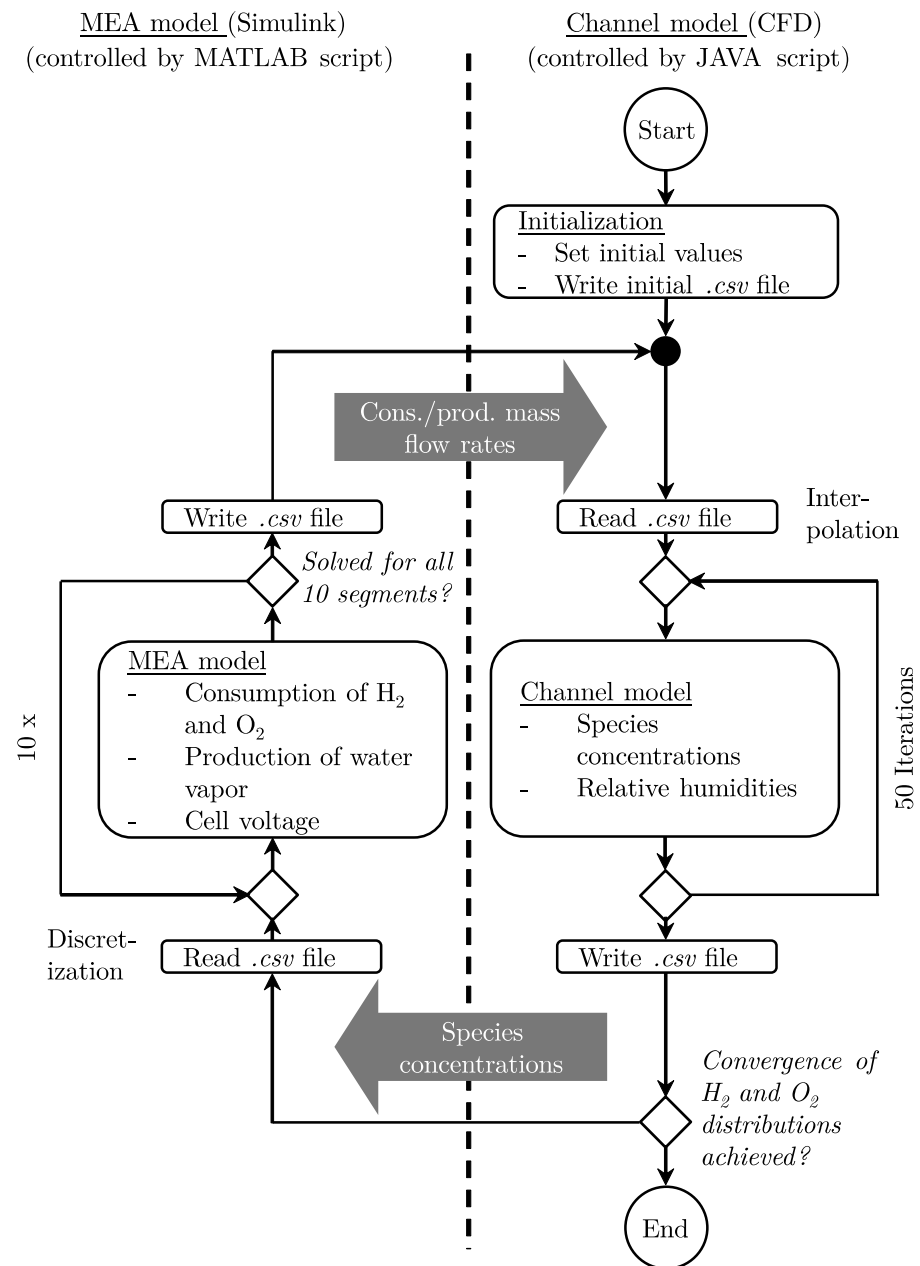


Figure 3. Algorithm scheme for coupling the one-dimensional MEA model with the two-dimensional CFD model.

3.4. Boundaries and Start Conditions

The model is validated against measurements of a PEM fuel cell on a test bench. For the best agreement between the experiments and the simulations, the conditions on the test bench and the operating strategy must be reproduced as well as possible in the simulations. The operating strategy of the fuel cell system is realized by the fuel cell control unit (FCCU). The stoichiometries on the anode and cathode sides decrease with increasing current density:

$$\lambda_A = 1.777 + 11.47 \cdot \exp\left(-\frac{i_{cell}}{0.04938}\right) \quad (19)$$

$$\lambda_C = 1.838 + 9.586 \cdot \exp\left(-\frac{i_{cell}}{0.06396}\right) \quad (20)$$

At the same time, the inlet gas pressures on both sides are continuously elevated as the required current density increases. The anode pressure is slightly higher than the cathode pressure:

$$p_A = 4.111 \cdot 10^4 \cdot i_{cell}^2 + 2.584 \cdot 10^4 \cdot i_{cell} + 1.207 \cdot 10^5 \quad (21)$$

$$p_C = 3.559 \cdot 10^4 \cdot i_{cell}^2 + 9.586 \cdot 10^4 \cdot i_{cell} + 1.039 \cdot 10^5 \quad (22)$$

4. Results and Discussion

4.1. Validation against Measurements

The model is validated against a measured polarization curve of a PEM fuel cell. The measurements were performed at the Center for Mobile Propulsion (cmp) of the Chair of Thermodynamics of Mobile Energy Conversion Systems (tme) of RWTH Aachen University. The results can be seen in Figure 4a.

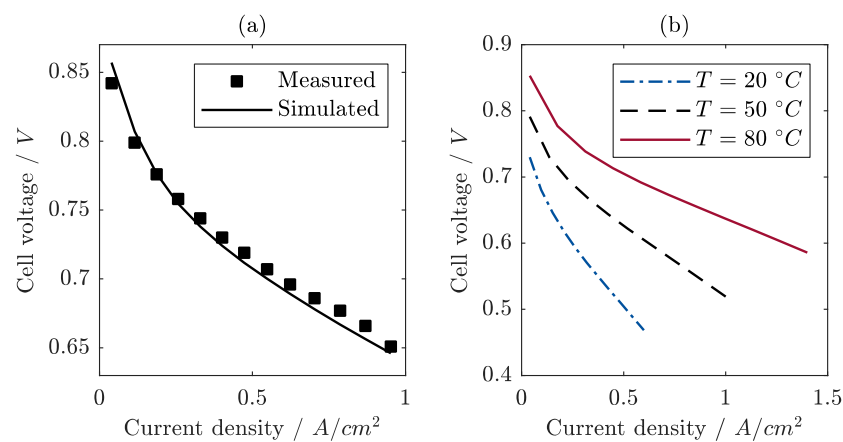


Figure 4. (a) Comparison between measured and simulated polarization curves at 50 °C; (b) Simulated polarization curves for operating temperatures of 20 °C, 50 °C, and 80 °C (the smallest measured current density is 0.05 A/cm², therefore operation in OCV is not investigated).

The comparison shows that the built model can calculate the behavior of the fuel cell very well. At small current densities, the model slightly overestimates the voltage, but the deviations from the measured voltages are small at medium and high current densities.

Figure 4b shows simulated polarization curves for the operating temperatures of 20 °C, 50 °C, and 80 °C. As the operating temperature decreases, the cell voltages become smaller. The rate of the electrochemical reactions depends on the temperature. At low temperatures, the transport processes and reaction rates that take place become slower, so that the overvoltages required to achieve the desired current density become larger. As a result, the cell voltage decreases.

4.2. Species Concentrations in Gas Channels during Operation

Figure 5 shows the distribution of the partial pressures of hydrogen on the anode side and oxygen on the cathode side in the gas channels. The length and height of the channels are shown dimensionless. A dimensionless channel length of 0 corresponds to the beginning of the respective gas channel, and a dimensionless channel length of 1 corresponds to the ending. This also applies to the dimensionless channel height. The dashed line corresponds to the respective surface of the GDL, i.e., the surface through which the exchange with the MEA model occurs. The partial pressures are calculated at a current density of $i'' = 0.952 \text{ A cm}^{-2}$ and a temperature of 80 °C.

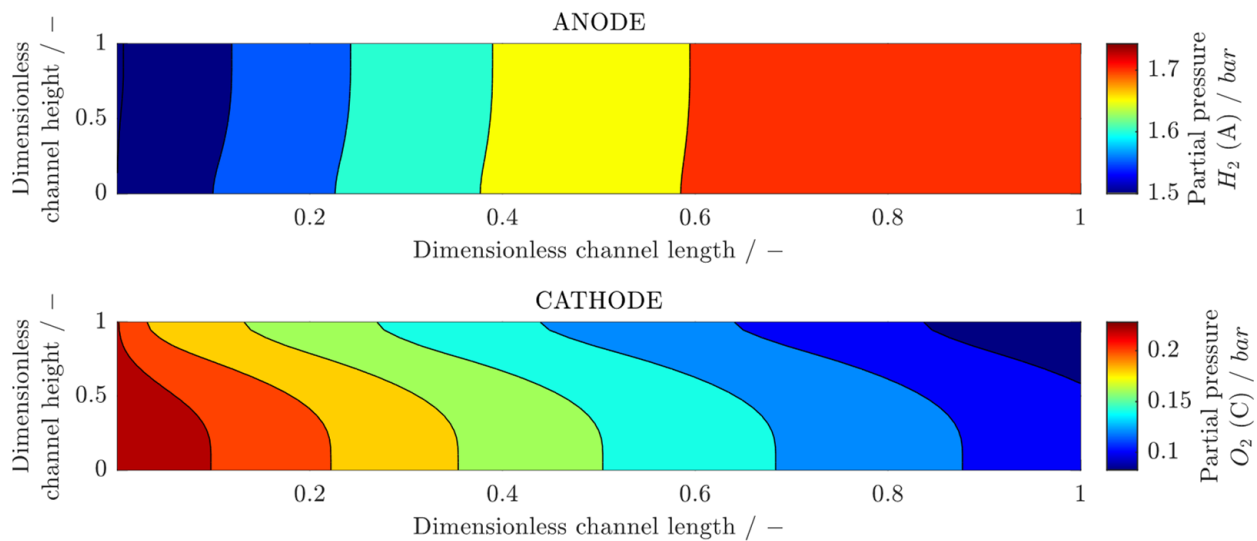


Figure 5. Partial pressure of hydrogen on the anode and oxygen on the cathode side in the gas channels. Channel length and height are shown dimensionless ($i'' = 0.952 \text{ Acm}^{-2}$, $T = 80 \text{ }^\circ\text{C}$, $\text{RH}_{\text{A,C}} = 70\%$).

Due to the consumption of hydrogen and oxygen during the operation of the cells, the partial pressures decrease along the length of the gas channels. In addition, the partial pressures also change in the height direction, with the lowest pressures of H_2 and O_2 being reached on the surfaces of the GDLs, respectively. The gradients in the height direction occur because the consumption of the gases and the exchange with the MEA model occur on the surfaces of the GDLs, respectively. The transport of gases in the gas channels is convective and diffusive. In the longitudinal direction of the channels, convective transport predominates due to the high flow velocity. Due to laminar flow, there are no flow velocities in the width and height directions of the channels, so convective transport does not happen in these directions. Therefore, the transport occurs across the channel length exclusively diffusively. The curves of the profile lines of the partial pressures shown result from the superposition of both types of transport. Due to the laminar flow in a longitudinal direction, the flow velocity is maximum in the center of the channels and minimum at the walls and the GDL surfaces. As a result, a parabolic velocity profile is formed. The diffusive transport in the direction of the GDL surfaces would cause linear progressions of the profile lines of the partial pressures if no flow existed in the channels. The superposition of convective transport (parabolic profile) and diffusive transport (linear profile) results in the partial pressure profiles shown in Figure 5.

4.3. Influence of Operating Temperature and Current Density

In this section, we examine how the operating temperature and current density influence the molar fractions of the gas species hydrogen and water vapor in the anode gas channel and oxygen and water vapor in the cathode gas channel, as well as the relative humidities. Operating temperatures of $20 \text{ }^\circ\text{C}$, $50 \text{ }^\circ\text{C}$, and $80 \text{ }^\circ\text{C}$ are considered. In Figures 6–8, the molar fractions and relative humidities as a function of current density are plotted versus the dimensionless channel length.

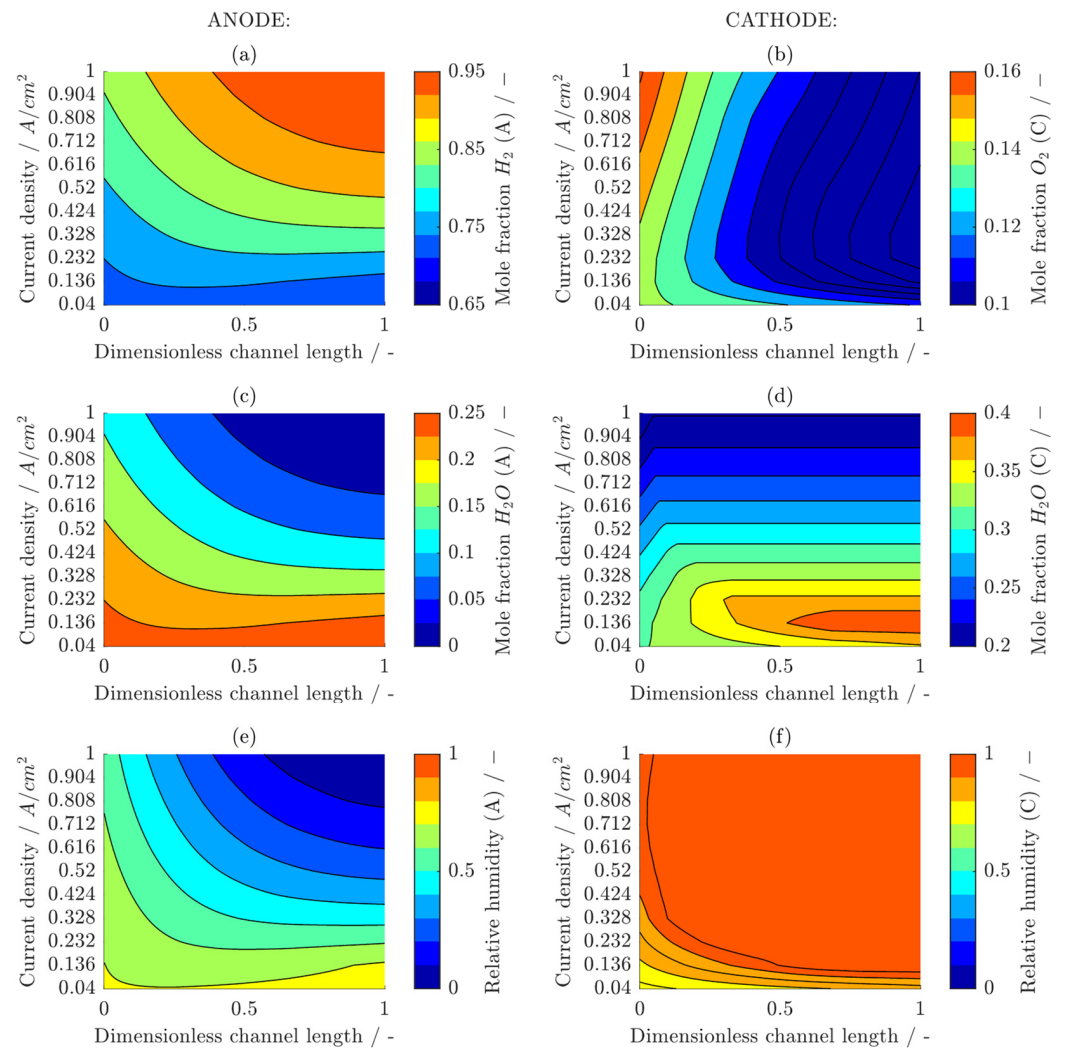


Figure 6. Mole fractions of hydrogen (a), oxygen (b), and water vapor (c,d) and relative humidities (e,f) in anode and cathode gas channels are shown as a function of current density ($T = 80\text{ }^{\circ}\text{C}$, $\text{RH}_{\text{A,C}} = 70\%$).

For all operating temperatures considered, it is obvious that the molar fractions of the gas species are already strongly dependent on the current density at the gas channel inlets. Since the pressure in the anode and cathode is set higher as the current density increases (cf. Equations (21) and (22)), but the relative humidities and, due to the same operating temperature, the saturated vapor pressure at the inlet are the same, the composition of the gas mixtures entering the cell changes. As the anode and cathode pressures increase, the fractions of hydrogen and oxygen increase, and the molar fractions of water vapor decrease. In subdiagrams (e) and (f) of Figures 6–8, it can be seen that despite a constant boundary condition of 70% RH, the humidities at the inlets of the gas channels vary significantly as a function of current density. These differences occur because the gas channels are extended at the inlets and outlets (cf. Section 3). Due to the mass transfer, the molar fractions also change slightly in the inlet extensions, although no exchange with the MEA model takes place there yet.

At a temperature of $80\text{ }^{\circ}\text{C}$, it can be seen that at high current densities, the hydrogen fraction increases despite the high consumption (Figure 6a, e.g., $i'' = 1.4\text{ A cm}^{-2}$). In this case, the electro-osmotic drag is so high that water is transported from the anode to the cathode, and, due to the decreasing water vapor fraction, the fraction of hydrogen must increase.

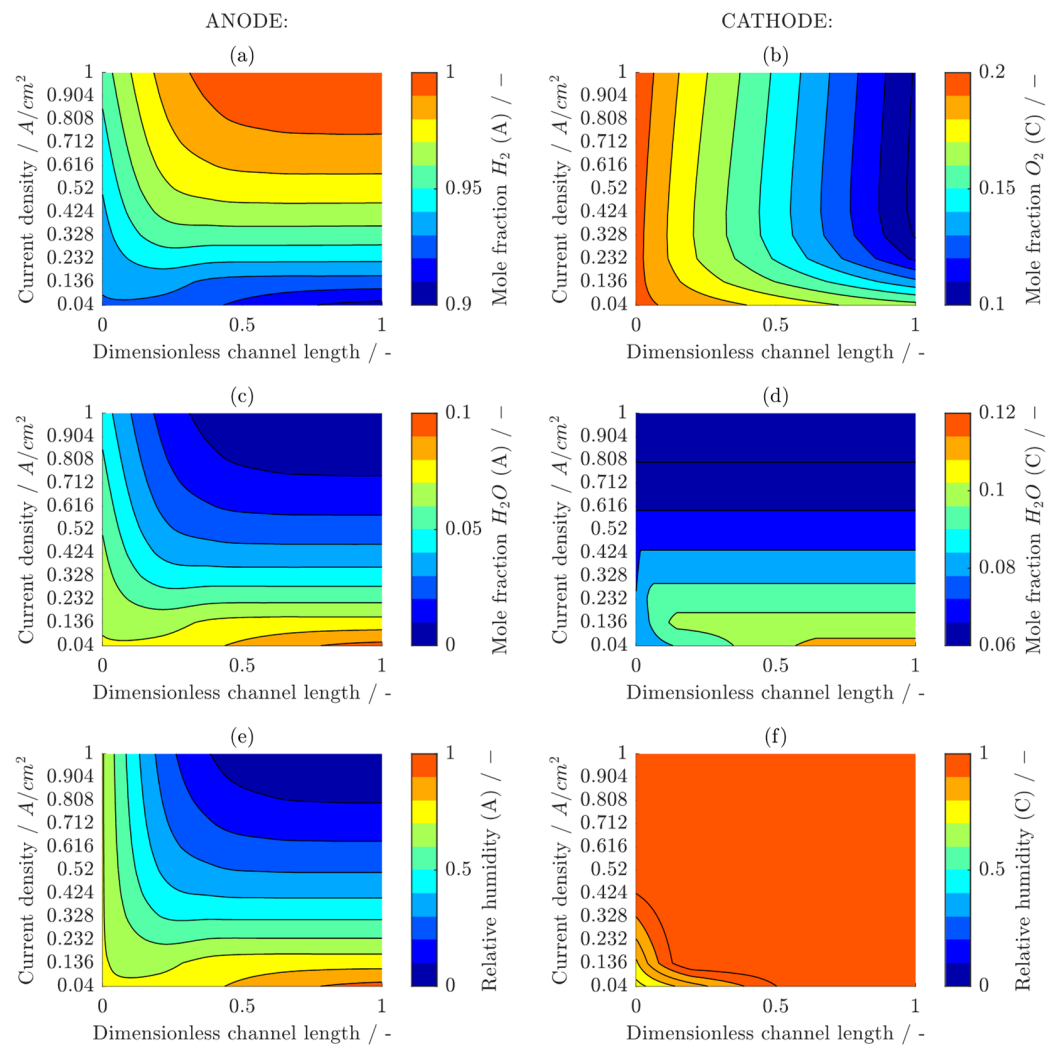


Figure 7. Mole fractions of hydrogen (a), oxygen (b), and water vapor (c,d) and relative humidities (e,f) in anode and cathode gas channels are shown as a function of current density and dimensionless channel length ($T = 50\text{ }^\circ\text{C}$, $RH_{A,C} = 70\%$).

Due to the consumption of hydrogen, the mass flow rate in the channel becomes smaller, which means that the flow velocity is decelerated.

Figure 6a further shows that at a small current density of, for example, $i'' = 0.176\text{ A cm}^{-2}$, the hydrogen fraction is small at the beginning of the channel, increases slightly toward the middle, and becomes smaller again toward the end. In parallel, the fraction of water vapor is initially smaller and becomes larger again toward the end of the gas channel. The reason for this phenomenon is again the interaction between the water vapor fraction, which is influenced by electro-osmotic drag and back diffusion, and the consumption of hydrogen. In the first half of the channel, the water vapor fraction decreases due to the electro-osmotic drag as water is transported to the cathode. As a result, the fraction of hydrogen becomes larger. As the humidity on the anode side decreases, the mass flow of water reaching the anode side due to concentration-driven back diffusion becomes larger. Since the electro-osmotic drag is low at lower current densities, an equilibrium between the electro-osmotic drag and the back diffusion can be established at the end of the gas channel so that the amount of water in the anode remains approximately the same in the back part of the channel. As hydrogen is consumed by the hydrogen oxidation reaction, the amount of hydrogen in the back part of the channel decreases. If the amount of water in the anode remains constant, the water vapor content must increase in return. Even at low current densities, this causes a deceleration of the flow velocity.

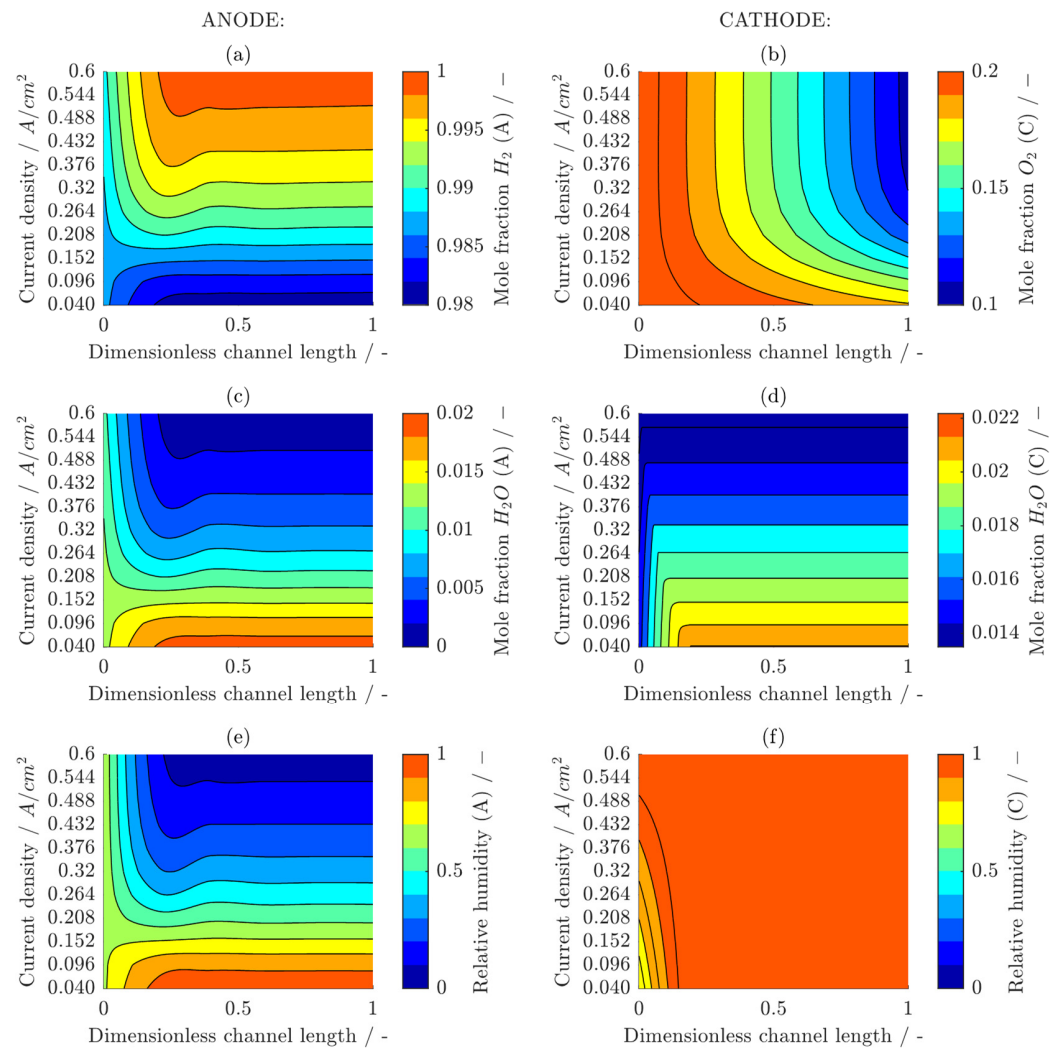


Figure 8. Mole fractions of hydrogen (a), oxygen (b), and water vapor (c,d) and relative humidities (e,f) in anode and cathode gas channels are shown as a function of current density and dimensionless channel length ($T = 20\text{ }^{\circ}\text{C}$, $\text{RH}_{A,C} = 70\%$).

In the gas channel of the cathode, the oxygen fraction decreases continuously over the length at high current densities due to consumption, and at the same time, the fraction of water vapor increases due to the production of water and the transport from the anode to the cathode. As soon as the partial pressure of water vapor reaches saturation vapor pressure, the gas is saturated and liquid water condenses. When the saturation state is reached, the relative humidity is equal to $\text{RH} = 1$. In Figure 6f, it can be seen that condensation of liquid water occurs more at the inlet of the gas channel as the current density increases. Since more product water is formed at high current densities and more water is transported through the membrane to the cathode by the electro-osmotic drag, saturation is reached more quickly. At very low current densities, e.g., $i'' = 0.04\text{ A cm}^{-2}$, saturation is not reached, so no liquid water is formed. In the saturation state, the molar fraction of water vapor also no longer changes. This is shown in Figure 6d. However, the mass fraction at saturation varies with the current density, since this depends largely on the pressure in the channel, which increases with increasing current density. Since a relative humidity of $\text{RH} = 1$ (saturation) cannot be exceeded, at a current density of about $i'' = 0.136\text{ A cm}^{-2}$ in the back channel region, the molar fraction of water vapor is at its maximum. For smaller and larger current densities, the water vapor fractions are smaller. This maximum occurs because at smaller gas pressures (achieved at smaller current densities), the molar fraction of water vapor at saturation is higher, but at too small

current densities (e.g., $i'' = 0.04 \text{ A cm}^{-2}$) too little water is produced to achieve saturation. At a temperature of $80 \text{ }^\circ\text{C}$, no liquid water condenses in the gas channel of the anode because saturation is not achieved at any current density.

The plots of the molar fractions and relative humidities at a temperature of $50 \text{ }^\circ\text{C}$ in Figure 7 are very similar to the plots at $80 \text{ }^\circ\text{C}$. Because of the lower temperature, the saturated vapor pressure is smaller, so the saturation state is reached more quickly, and the first liquid water droplets are reached earlier in the channel and at lower current densities. As shown in Figure 7e, at a temperature of $50 \text{ }^\circ\text{C}$ and a very small current density of $i'' = 0.04 \text{ A cm}^{-2}$, water condenses in the back part of the anode gas channel because the electro-osmotic drag is low and thus much water enters the anode by diffusion. At higher current densities, water transport from the anode to the cathode dominates. It can be seen that for current densities greater than 0.808 A cm^{-2} , the anode dries out completely in the back part as the relative humidity drops to a value of 0. Water condenses in the cathode gas channel at this temperature at any current density. At current densities greater than 0.424 A cm^{-2} , the water vapor content is so high that liquid water is already formed at the inlet of the channel (Figure 7f).

At a temperature of $20 \text{ }^\circ\text{C}$, the maximum current density is $i'' = 0.6 \text{ A cm}^{-2}$. Since the saturation vapor pressure is even lower, more condensation occurs, especially at the anode, despite smaller current densities. Nevertheless, drying in the back part of the channel is still possible at high current densities (cf. Figure 8).

The simulation results show that for a cold start, the formation of liquid water in the gas channels cannot be avoided only by the choice of current density. At low temperatures and low current densities, the water condenses in the gas channel of the cathode only in the rear part, and the amount of water is also smaller, but due to the low electro-osmotic drag, a lot of water is transported through back diffusion to the anode, so that water condenses there. High current densities lead to liquid water formation in the entire gas channel of the cathode, but at low temperatures, high current densities also lead to drying out of the rear areas of the gas channel of the anode.

5. Conclusions

In this study, the construction of a coupled model between a one-dimensional model of the MEA and a two-dimensional CFD model of the gas channels is described. Both models are controlled by individual scripts, and the data exchange is realized periodically via .csv files. The model is validated with measurement data. Simulations are carried out to find out how the concentrations of the gas species in the channels change at different temperatures and current densities. In addition, the conditions under which saturation and, thus, condensation of liquid water occur are investigated.

The following statements can be concluded from the investigations:

- The presented coupling between a one-dimensional model of the MEA and a two-dimensional model of the gas channels is a well-suited method to simulate the behavior of a PEM fuel cell.
- The simulations show that the interaction between the electro-osmotic drag and the back diffusion of water through the membrane strongly influences the concentrations of the gas species and the formation of liquid water.
- The water vapor contents and the amounts of liquid water in the gas channels are influenced by the current density, but at low operating temperatures and during cold starts, the formation of liquid water cannot be avoided by the choice of current density alone.
- We conclude that during a cold start, an attempt must be made to heat up the cells as quickly as possible so that only a small amount of liquid water can condense out.

In further investigations, the two-dimensional CFD model of the gas channels will be replaced by a three-dimensional model. The coupling algorithm is then extended so that transient simulations can be performed. The model is then used to simulate various cold-start procedures. This is conducted to evaluate whether the fuel cell also behaves

in dynamic operation at low temperatures, as expected from the studies presented for steady-state operating points.

Author Contributions: Conceptualization, M.S.; methodology, M.S.; software, F.M.; validation, F.M. and S.D.; formal analysis, M.S.; investigation, M.S. and F.M.; resources, M.S. and F.M.; data curation, F.M.; writing—original draft preparation, M.S.; writing—review and editing, F.M. and S.D.; visualization, M.S.; supervision, S.P.; project administration, S.P.; funding acquisition, S.P. All authors have read and agreed to the published version of the manuscript.

Funding: This research is part of the research project X-EMU: Development and Validation of a High-Performance Fuel Cell Propulsion System for Hybrid EMU railcars in a Modular Traction Design System and was funded by the Federal Ministry of Transport and Digital Infrastructure of Germany (BMVI), grant number 03B10502.

Data Availability Statement: The data presented in this study are available on request from the corresponding author. The data are not publicly available due to confidentiality.

Acknowledgments: Simulations were performed with computing resources granted by RWTH Aachen University.

Conflicts of Interest: The authors declare no conflicts of interest.

Nomenclature

U_{Cell}	Cell voltage	V
U_{Nernst}	Nernst voltage	V
ΔU_{mix}	Mixed voltage losses	V
ΔU_{act}	Activation overvoltage	V
ΔU_{Ω}	Ohmic losses	V
T	Cell temperature	K
p_i	Partial pressure species i	Pa
i''	Current density	A cm ⁻²
M_i	Molar mass species i	kg mol ⁻¹
$\dot{m}''_{prod,i}$	Mass flow production	kg m ⁻² s ⁻¹
$\dot{m}''_{cons,i}$	Mass flow consumption	kg m ⁻² s ⁻¹
$\dot{m}''_{mem,i}$	Mass flow through the membrane	kg m ⁻² s ⁻¹
V_{CL}	Volume catalyst layer	m ³
λ_{mem}	Membrane water content	-
ρ_{gas}	Density gas	kg m ⁻³
\vec{v}_{gas}	Flow velocity	m s ⁻¹
S_i	Source term species i	kg m ⁻³ s ⁻¹
μ	Viscosity gas	Pa s
X_i	Molar fraction species i	-
Y_i	Mass fraction species i	-
p_{sat}	Saturation vapor pressure	Pa
$\lambda_{A,C}$	Stoichiometries	-

Appendix A

Table A1. Parameter values of the CFD model.

Symbol	Parameter	Value	Unit	Source
ΔG_R^0	Standard reaction enthalpy	-237,130	J mol ⁻¹	[27]
ΔS_R^0	Standard reaction entropy	-44.405	J mol ⁻¹ K ⁻¹	[27]
F	Faraday's constant	96,485.34	A s mol ⁻¹	-
n	Electrochemical valence	2	-	[26]
α	Charge transfer coefficient	1	-	[26]
p^0	Standard pressure	1	bar	-

Table A1. Cont.

Symbol	Parameter	Value	Unit	Source
$i''_{0,ORR}$	Exchange current density	1.24×10^{-4}	$A\ cm^{-2}$	[15]
$\Delta E_{act,ORR}$	Activation energy	7900	$J\ mol^{-1}$	[32]
$R_{elec,GDL,BPP}$	Electrical contact resistance	4.2	Ω	assum.
ϵ	Porosity	0.5	-	[22]
τ	Tortuosity	3.725	-	[22]
C	Condensation constant	6×10^{-3}	$s\ m^{-2}$	assum.
d_{mem}	Thickness membrane	1.5×10^{-5}	m	meas.
d_{ACL}	Thickness ACL	1.0×10^{-5}	m	meas.
d_{CCL}	Thickness CCL	1.2×10^{-5}	m	meas.
d_{AGDL}	Thickness AGDL	2.5×10^{-4}	m	meas.
d_{CGDL}	Thickness CGDL	2.5×10^{-4}	m	meas.
T_{ref}	Reference temperature	353	K	[22]

References

- Balliet, R.J. *Modeling Cold Start in a Polymer-Electrolyte Fuel Cell*; University of California: Berkeley, CA, USA, 2010.
- Al-Baghdadi, M.A.S. Mechanical behaviour of membrane electrode assembly (MEA) during cold start of PEM fuel cell from subzero environment temperature. *Int. J. Energy Environ.* **2015**, *6*, 107.
- Yan, S.; Yang, M.; Sun, C.; Xu, S. Liquid Water Characteristics in the Compressed Gradient Porosity Gas Diffusion Layer of Proton Exchange Membrane Fuel Cells Using the Lattice Boltzmann Method. *Energies* **2023**, *16*, 6010. [\[CrossRef\]](#)
- Springer, T.E.; Zawodzinski, T.A.; Gottesfeld, S. Polymer Electrolyte Fuel Cell Model. *J. Electrochem. Soc.* **1991**, *138*, 2334–2342. [\[CrossRef\]](#)
- Zawodzinski, T.A.; Derouin, C.; Radzinski, S.; Sherman, R.J.; Smith, V.T.; Springer, T.E.; Gottesfeld, S. Water Uptake by and Transport Through Nafion® 117 Membranes. *J. Electrochem. Soc.* **1993**, *140*, 1041–1047. [\[CrossRef\]](#)
- Bernardi, D.M.; Verbrugge, M.W. Mathematical model of a gas diffusion electrode bonded to a polymer electrolyte. *AIChE J.* **1991**, *37*, 1151–1163. [\[CrossRef\]](#)
- Bernardi, D.M.; Verbrugge, M.W. A Mathematical Model of the Solid-Polymer-Electrolyte Fuel Cell. *J. Electrochem. Soc.* **1992**, *139*, 2477. [\[CrossRef\]](#)
- Fuller, T.F.; Newman, J. Water and Thermal Management in Solid-Polymer-Electrolyte Fuel Cells. *J. Electrochem. Soc.* **1993**, *140*, 1218. [\[CrossRef\]](#)
- Nguyen, T.V.; White, R.E. A Water and Heat Management Model for Proton-Exchange-Membrane Fuel Cells. *J. Electrochem. Soc.* **1993**, *140*, 2178–2186. [\[CrossRef\]](#)
- Yuan, W.-W.; Ou, K.; Kim, Y.-B. Alleviating the performance degradation of fuel cells caused by the uneven distribution of internal physical fields. *Energy Convers. Manag.* **2020**, *225*, 113449. [\[CrossRef\]](#)
- Gurau, V.; Liu, H.; Kakaç, S. Two-dimensional model for proton exchange membrane fuel cells. *AIChE J.* **1998**, *44*, 2410–2422. [\[CrossRef\]](#)
- Dutta, S.; Shimpalee, S.; Van Zee, J. Three-dimensional numerical simulation of straight channel PEM fuel cells. *J. Appl. Electrochem.* **2000**, *30*, 135–146. [\[CrossRef\]](#)
- Berg, P.; Promislow, K.; Pierre, J.S.; Stumper, J.; Wetton, B. Water Management in PEM Fuel Cells. *Electrochim. Acta* **2004**, *151*, A341. [\[CrossRef\]](#)
- Natarajan, D.; van Nguyen, T. Three-dimensional effects of liquid water flooding in the cathode of a PEM fuel cell. *J. Power Sources* **2003**, *115*, 66–80. [\[CrossRef\]](#)
- Natarajan, D.; van Nguyen, T. A Two-Dimensional, Two-Phase, Multicomponent, Transient Model for the Cathode of a Proton Exchange Membrane Fuel Cell Using Conventional Gas Distributors. *J. Appl. Electrochem.* **2001**, *148*, A1324. [\[CrossRef\]](#)
- Abdin, Z.; Webb, C.; Gray, E. PEM fuel cell model and simulation in Matlab–Simulink based on physical parameters. *Energy* **2016**, *116*, 1131–1144. [\[CrossRef\]](#)
- Chen, Y.-S.; Peng, H. A segmented model for studying water transport in a PEMFC. *J. Power Sources* **2008**, *185*, 1179–1192. [\[CrossRef\]](#)
- Mueller, F.; Brouwer, J.; Kang, S.; Kim, H.-S.; Min, K. Quasi-three dimensional dynamic model of a proton exchange membrane fuel cell for system and controls development. *J. Power Sources* **2007**, *163*, 814–829. [\[CrossRef\]](#)
- Chen, Y.-S.; Peng, H. Predicting current density distribution of proton exchange membrane fuel cells with different flow field designs. *J. Power Sources* **2011**, *196*, 1992–2004. [\[CrossRef\]](#)
- Schumacher, J.O.; Eller, J.; Sartoris, G.; Colinart, T.; Seyfang, B.C. 2+1D modelling of a polymer electrolyte fuel cell with glassy-carbon microstructures. *Math. Comput. Model. Dyn. Syst.* **2012**, *18*, 355–377. [\[CrossRef\]](#)
- Pant, L.M.; Gerhardt, M.R.; Macauley, N.; Mukundan, R.; Borup, R.L.; Weber, A.Z. Along-the-channel modeling and analysis of PEFCs at low stoichiometry: Development of a 1+2D model. *Electrochimica Acta* **2019**, *326*, 134963. [\[CrossRef\]](#)
- Shan, Y.; Choe, S.-Y. A high dynamic PEM fuel cell model with temperature effects. *J. Power Sources* **2005**, *145*, 30–39. [\[CrossRef\]](#)

23. Baschuk, J.; Li, X. A general formulation for a mathematical PEM fuel cell model. *J. Power Sources* **2005**, *142*, 134–153. [[CrossRef](#)]
24. Pasricha, S.; Shaw, S.R. A Dynamic PEM Fuel Cell Model. *IEEE Trans. Energy Convers.* **2006**, *21*, 484–490. [[CrossRef](#)]
25. Pathapati, P.R.; Xue, X.; Tang, J. A new dynamic model for predicting transient phenomena in a PEM fuel cell system. *Renew. Energy* **2005**, *30*, 1–22. [[CrossRef](#)]
26. Meng, H. A PEM fuel cell model for cold-start simulations. *J. Power Sources* **2007**, *178*, 141–150. [[CrossRef](#)]
27. Scholz, H. *Modellierung und Untersuchung von Flutungsphänomenen in Niedertemperatur-PEM-Brennstoffzellen*; AutoUni-Schriftenreihe v.82; Logos Verlag: Berlin, Germany, 2015.
28. Sun, C.; Negro, E.; Vezzu, K.; Pagot, G.; Cavinato, G.; Nale, A.; Bang, Y.H.; Di Noto, V. Hybrid inorganic-organic proton-conducting membranes based on SPEEK doped with WO₃ nanoparticles for application in vanadium redox flow batteries. *Electrochim. Acta* **2019**, *309*, 311–325. [[CrossRef](#)]
29. Siemens PLM Software. *Simcenter STAR-CCM+ Documentation*, Version 13.06; Siemens PLM Software: Plano, TX, USA, 2018.
30. Basu, S.; Wang, C.-Y.; Chen, K.S. Phase Change in a Polymer Electrolyte Fuel Cell. *J. Electrochem. Soc.* **2009**, *156*, B748–B756. [[CrossRef](#)]
31. Jiao, K.; Li, X. Effects of various operating and initial conditions on cold start performance of polymer electrolyte membrane fuel cells. *Int. J. Hydrogen Energy* **2009**, *34*, 8171–8184. [[CrossRef](#)]
32. Yao, L.; Peng, J.; Zhang, J.-B.; Zhang, Y.-J. Numerical investigation of cold-start behavior of polymer electrolyte fuel cells in the presence of super-cooled water. *Int. J. Hydrogen Energy* **2018**, *43*, 15505–15520. [[CrossRef](#)]

Disclaimer/Publisher's Note: The statements, opinions and data contained in all publications are solely those of the individual author(s) and contributor(s) and not of MDPI and/or the editor(s). MDPI and/or the editor(s) disclaim responsibility for any injury to people or property resulting from any ideas, methods, instructions or products referred to in the content.